Determination of the Anisotropic Elastic Properties of Rocksalt $Ge_2Sb_2Te_5$ by XRD, Residual Stress and DFT

Raimondo Cecchini[†,1], *Krisztian Kohary*[‡], *Asunción Fernández*[†], *Marcello Cabibbo*[§], *Arnaud Marmier*[‡,*]

[†]Instituto de Ciencia de Materiales de Sevilla, CSIC-Universidad de Sevilla, Avenida Américo Vespucio 49, 41092 -Seville, Spain.

[‡]College of Engineering, Mathematics and Physical Sciences, University of Exeter, Exeter EX4 4QF, United Kingdom.

[§]Department of Mechanical Engineering, Università Politecnica delle Marche, via Brecce Bianche, 60131, Ancona, Italy.

KEYWORDS Chalcogenide films, phase change, optical storage, random access memory, elasticity

---

[1] Presently at Laboratorio MDM, IMM-CNR, Unità di Agrate Brianza, Via C. Olivetti 2, 20864 Agrate Brianza, (MB), Italy.

Abstract

The chalcogenide material $Ge_2Sb_2Te_5$ is the prototype phase-change material, with widespread applications for optical media and random access memory. However, the full set of its independent elastic properties has not yet been published. In this study, we determine the elastic constants of the rocksalt $Ge_2Sb_2Te_5$, experimentally by x-ray diffraction (XRD) and residual stress, and computationally by density functional theory (DFT). The stiffnesses (XRD-stress/DFT) in GPa are C_{11} = 41/58, C_{12} = 7/8 and C_{44} = 8/12 and the Zener ratio is 0.46/0.48. These values are important to understand the effect of elastic distortions and non-melting processes on the performances of increasingly small phase change data bits.

1. INTRODUCTION

Chalcogenide films have been employed in phase-change type optical storage media[1-2] (CD-RW, DVD-RW, Blu-Ray DVD) and, more recently, in phase-change random access memory (PCRAM) [3-5]. The Ge-Sb-Te (GST) system and in particular the $Ge_2Sb_2Te_5$ alloy (GST225), are amongst the most studied materials for optical and PCRAM devices. The importance of these chalcogenide alloys for advanced memory applications makes the determination of material properties, such as elastic ones, a critical issue. For example, thermal expansion during the transformation from crystalline to amorphous state can lead to an onset of pressures in the gigapascals range in the amorphous bits of PCRAMs [6-11]. This can have an important effect on device performance and reliability. Moreover, recent research [12-13] has shed new light into the crystalline to amorphous transition of GST225 and other chalcogenide alloys, highlighting the role of non-melting amorphization processes (dislocations and pressure driven). Elastic anisotropy in particular plays a key role in phase transformations and dislocation dynamics. It is also bound to become even more important in highly scaled future generation PCRAMs, as memory bits are shrunk to nanometric sizes, as in confined nanosized cells[14-15] or in proposed PCRAM based on chalcogenide nanowires[16-18] and consist of only a few crystallites that are unlikely to be isotropic. Full knowledge of the mechanical properties of these class of materials is therefore important for the understating of current devices and crucial for the design of more efficient PCRAMs. The detail of the elastic properties is also important for modelling at different scales. Multiphysics Finite Element based simulations of devices rely on constitutive models that include elastic properties. At the atomic scale, elastic constants provide observables to check the quality of a model or to parameterise new ones.

Despite their relevance to real systems and devices, no measurements of the full set of face-centered cubic (FCC) GST225 elastic properties have been reported to date. Published results are generally limited to the bulk modulus (K)[7, 19-21], with a few mentions of the biaxial (Y)and Young's moduli (E)[8, 11, 22]. Recent simulations have indicated that the closely related material $Ge_1Sb_2Te_4$ (GST124) exhibits significant elastic anisotropy with a Zener ratio (A) of 0.24 [23]. The results for GST124 are more detailed than for GST225, with a full set of elastic constants from density functional theory (DFT) calculations [23] and a partial set (isotropic approximation) from Brillouin Light Scattering (BLS) [24]. Recently, the elastic coefficients of stable trigonal GST225 have been calculated by DFT[25]. The picture resulting from these results is that the data are almost equally divided between two hypotheses: high compressibility with K around 20 GPa and low compressibility with K around 40 GPa.

The following section presents the methods used to measure and calculate the elastic properties. Our experimental approach, a combination of x-ray diffraction and residual stress measurements, has not been used previously to directly measure elastic tensors, and is introduced with much detail. We then present exhaustive results for elastic properties and show that the experimental and computational results are in very good agreement. Finally we demonstrate that elastic anisotropy must be taken into account.

2. EXPERIMENTAL AND COMPUTATIONAL METHODS

Under the deposition conditions used in the present work, GST225 adopts a distorted rocksalt like structure, where the Te atoms occupy one FCC sub-lattice, while the other FCC sub-lattice is populated by Ge and Sb atoms, as well as vacancies (around 20%). Due to this essentially cubic structure, three elastic constants suffice to describe its elasticity. On the other hand, the

stochastic nature of the distribution of the Ge/Sb/vacancies sites makes simulating GST225 a delicate problem, requiring averaging over different configurations.

2.1. Experimental Details. GST225 films were deposited on single crystal Si(100) substrates by direct-current magnetron sputtering from a target with composition Ge: Sb: Te = 2: 2: 5. Substrates temperature was kept at 130 ºC, deposition power was 0.5 kW and sputtering gas Ar pressure was 2 mTorr. Films were deposited with thicknesses of 700, 2000 and 3500 nm. We applied X-Ray diffraction (XRD) with fixed incidence angle and residual stress measurements by the curvature method on polycrystalline rocksalt GST225 films to measure the compliances terms (S_{ij}) from the Reuss' model [26]. XRD measurements are often used for the evaluation of the residual stress of thin films, and they are occasionally[27] combined with the curvature method to check the validity of elastic constants. We are not aware of the use of combined XRD-stress measurement to determine elastic constants directly. The residual planar stress ($\sigma_{\parallel}$) acting on the films was evaluated by measuring the curvature radius of the samples before (R) and after (R') film deposition in different directions, to confirm the rotational symmetry of the state of stress, and by applying the Stoney's equation [28-29]: $\sigma_{\parallel} = M_{Si(100)} \cdot t^2_{Si(100)}/t_f \cdot 1/6(R' - R)$, where t_f is the thickness of the GST film and $t^2_{Si(100)}$= 730 μm and $M_{Si(100)}$ = 180.3 GPa are the thickness and the biaxial modulus of the Si(100) substrate. The values of the curvature radius were obtained from the maximum samples deflections (h) measured by a Mahr ® Surf XR-20 stylus profilometer along traces of length L= 17.5 mm, by $R = L^2/8h$. The resulting $\sigma_{\parallel}$ values were (-0.30 ± 0.03), (-0.17 ± 0.02) and (-0.15 ± 0.02) GPa for the 700, 2000 and 3500 nm thick films respectively. The XRD patterns were recorded in parallel beam optics configuration (parallel plate collimator 0.27°) and Bragg-Brentano para-focusing geometry by a Panalytical ® X'PERT-PRO diffractometer operated at 40 kV and 40 mA with Cu Kα radiation with fixed

angles of incidence (α), with values of 1°, 5°, 10°, 15°, 20°, 30° and 45° and 2θ scans from 45° to 80 ° with step size 0.025°. The XRD patterns recorded on 2000 nm thick film for $\alpha = 10°$ are reported in Figure 1.

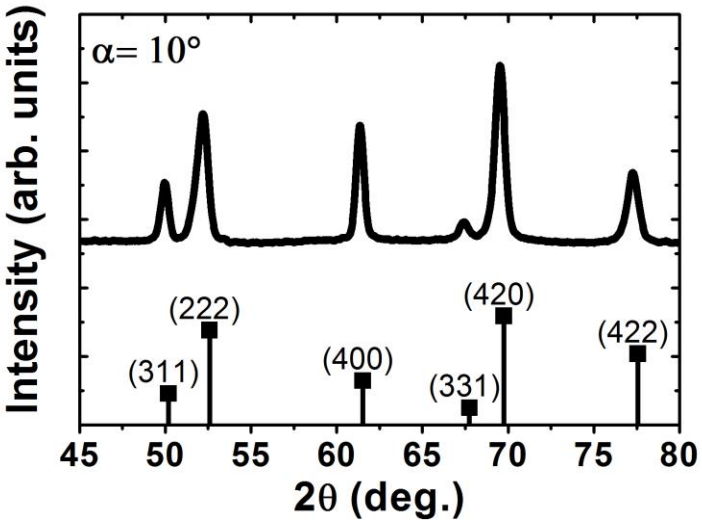

Figure 1. XRD patterns recorded for GST225 2000 nm film with fixed angle of incidence α = 10°. The positions and relative intensities of FCC GST225 peaks[30] are also displayed.

As can be seen by comparison with previously reported XRD measurements [30], the films are polycrystalline with a FCC structure. Similarly to in Grazing Angle X-Ray Diffraction (GIXRD), in XRD with a fixed α different inclination angles (ψ) are obtained, according to: $\psi^{hkl} = \theta^{hkl} - \alpha$, where θ_{hkl} is the diffraction angle for the (hkl) plane. A fixed angle of incidence allows for better control of the x-ray penetration depth. However, while in GIXRD low values of α are generally used to increase the signal from very thin films, we used a relatively large α range in order to obtain a large enough range of ψ^{hkl} and allow for the measurement of the elastic properties. The determination of the θ_{hkl} values was done by Lorentzian curve-fitting of each Bragg peak of the XRD patterns. For each (hkl) plane with inclination ψ^{hkl}, the values of

the strained lattice constant ($a_{\psi^{hkl}}^{hkl}$) are given by the Bragg's equation: $a_{\psi^{hkl}}^{hkl} = \frac{\lambda_{Cu\,K\alpha}}{2\sin\theta^{hkl}}\sqrt{h^2k^2l^2}$. For macroscopically elastically isotropic materials subjected to rotationally symmetric biaxial stress, the relationship between strain, $\frac{a_{\psi^{hkl}}^{hkl}-a_0}{a_0}$ (where a_0 is the value of the unstrained lattice parameter) and $\sigma_{\parallel}$ is given by [31]

$$\frac{a_{\psi^{hkl}}^{hkl}-a_0}{a_0} = \left(2S_1^{hkl} + \frac{1}{2}S_2^{hkl}sin^2\psi^{hkl}\right)\sigma_{\parallel} \quad (1)$$

with and S_1^{hkl} and S_2^{hkl} the hkl-dependent diffraction elastic compliances. In terms of the Reuss' model, the independent terms of the compliance tensor S_{11}, S_{12} and S_{44} are related to the hkl-dependent diffraction compliances (S_1^{hkl}, $\frac{1}{2}S_2^{hkl}$) by the equations[31]

$$S_1^{hkl} = S_{12} + S_0\Gamma(hkl) \quad (2)$$

and

$$\frac{1}{2}S_2^{hkl} = S_{11} - S_{12} - 3S_0\Gamma(hkl) \quad (3),$$

where $S_0 = S_{11} - S_{12} - S_{44}/2$ and $\Gamma(hkl) = (h^2k^2 + k^2l^2 + l^2h^2)/(h^2 + k^2 + l^2)^2$ is the orientation factor for cubic materials. Replacing eq. (2) and (3) into eq. (1) leads to

$$a_{\psi^{hkl}}^{hkl} = a_0\left\{\left[2\left(S_{12} + S_0\Gamma(hkl)\right) + \left(S_{11} - S_{12} - 3S_0\Gamma(hkl)\right)sin^2\psi^{hkl}\right]\sigma_{\parallel} + 1\right\}. \quad (4)$$

The values of a_0, S_{11}, S_{12} and S_0 for GST225 were obtained by a weighted least-square fitting by eq. (4) of the measured $a_{\psi^{hkl}}^{hkl}$ and $sin^2\psi^{hkl}$ values for the different films and different a. The goodness of the fit can be estimated by comparing the measured $a_{\psi^{hkl}}^{hkl}$ with those calculated from eq. (4) with a_0, S_{11}, S_{12} and S_0 obtained from the fit (Figure 2). In order to make the plot legible, only the values relative to 700 nm and 3500 nm samples, α = 5° and 15° and reflections (400), (311), (420) and (222) are shown. Two important sources of experimental uncertainty in the procedure described above are represented by the measurement of residual stress by the

curvature method and by the possible presence of a gradient of the stress along the film thickness. It is generally observed that the uncertainty for this type of measurement is of the order of 10%. However, evaluation of the curvature of the samples after the film deposition can introduce relatively large errors, especially for the smallest thickness, where the change of curvature is relatively small. Moreover, the value measured by the curvature method represents the average residual stress of the films, while the stress might change throughout the film thickness. The diffracted signal might therefore come from a depth where the value of the stress differs from its average value. We used different values of incident angle in order to collect information from a wide range of films depths and average out the effect of stress gradients.

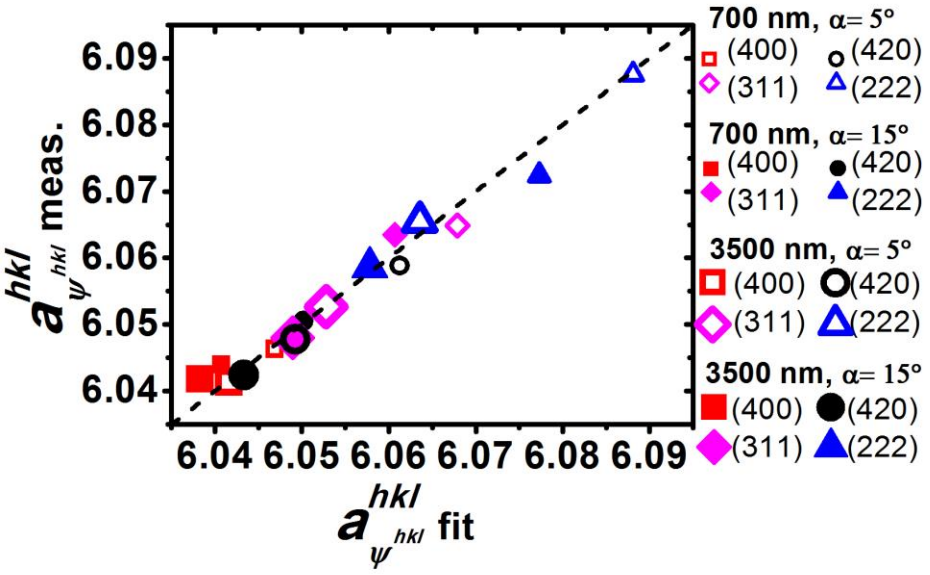

Figure 2. (color online) Plot of XRD measured strained lattice constant values ($a_{\psi^{hkl}}^{hkl}\ meas.$) vs. those calculated from eq. (4) with a_0, S_{11}, S_{12} and S_0 obtained from the fit ($a_{\psi^{hkl}}^{hkl}\ fit$). The dashed line indicates the expected unit slope.

2.2. Computational Details. We performed DFT simulations in the framework of the generalized gradient approximation (GGA) with Perdew-Burke-Ernzerhof (PBE) functional and projector augmented wave-method (PAW) potentials using the VASP software[32-35]. The calculations were performed with energy cutoff of 15 Ha and Monkhorst-Pack grids of 4×4×4 k-points. GST225 crystallizes in the FCC rocksalt system with two sublattices occupied by either Te atoms ("A" sublattice) or Ge/Sb atoms and vacancies ("B" sublattice). In order to conserve the somewhat awkward stoichiometry, we generated eight 36-atoms GST225 structures using a 2×2×5 replication of the "primitive" FCC unit cell (with one site for each of the two sublattices). The spatial distribution of Ge, Sb and vacancies in the "B" sublattice was determined by a random number generator. Eight such configurations were relaxed, and the full compliance tensors were calculated. Due to the random distribution in one sublattice, the relaxed supercells, and the associated elastic tensors, although quasi-cubic, do belong to the triclinic crystal system. The three cubic stiffnesses (C) are obtained by a direct averaging of the relevant triclinic stiffnesses ($C_{11}^{cub} = \left(\sum_{i=1,3} C_{ii}^{tri}\right)/3$, $C_{12}^{cub} = \left(\sum_{\substack{i=1,3 \\ j=1,3, j\neq i}} C_{ij}^{tri}\right)/6$, $C_{44}^{cub} = \left(\sum_{i=4,6} C_{ii}^{tri}\right)/3$). The errors quoted for these results are simply standard deviation errors from these averaging; they underestimate the actual errors inherent to DFT and are not directly comparable with the experimental errors.

2.3. Elasticity considerations. Due to the cubic symmetry imparted on the elastic tensors, the formulae to invert compliance and stiffnesses and to average the various moduli are quite simple. Likewise, the bulk modulus is easy to calculate (the linear compressibility of cubic crystals is always isotropic). On the other hand, a cubic system is not elastically isotropic and the angular dependence of Young's and biaxial moduli is more involved, and those of Poisson's

ratio (v) and shear modulus (G) are very heavy. We use the dedicated software ElAM[36] to carry out the tensor transformations and compute various representative values (minima, maxima, averages), as well as graphically represent the different values of an elastic property.

3. RESULTS AND DISCUSSION

The first and simplest quantity we address is the lattice parameter a_0 which is 6.035±0.001 Å from XRD-stress and 6.12 ±0.05 Å from DFT (agreement within 2%). In fact, it is not surprising that the DFT value is larger than the experimental one as the GGA functionals tend to overestimate lattice parameters, at 6.05 Å from[37] and 6.04 Å from[38] (conversely, the LDA functionals tends to underestimate lattice parameters, at 5.90 Å from[39]). The results are also very close to experimental values for GST225 *films* [30], where a_0 varies between 6.025 Å and 6.050 Å.

Table 1. Elastic properties (compliances, stiffnesses, Zener ratio, bulk modulus, Young's modulus, biaxial modulus, shear modulus and Poisson's ratio) of GST225 obtained from XRD-stress and PAW-DFT.

Properties	XRD-stress	DFT
S_{11} (TPa^{-1})	26 ± 3	18 ± 2
S_{12} (TPa^{-1})	-4 ± 1	-2 ± 1
S_{44} (TPa^{-1})	130 ± 10	83 ± 8
C_{11} (GPa)	41 ± 6	58 ± 4
C_{12} (GPa)	7 ± 4	8 ± 3
C_{44} (GPa)	8 ± 1	12 ± 1
A	0.45 ± 0.05	0.49 ± 0.1
K (GPa)	20 ± 5	25 ± 1
E (min-max) (GPa)	20-38 (±5)	31-56 (±3)
Y (min-max) (GPa)	25-45(±7)	38-64 (±4)
G (min-max) (GPa)	8-17(±1)	12-25 (±4)

ν (min-max) (GPa)	0.09-0.49(± 0.2)	0.07-0.45 (±0.02)

For the raw elastic constants, compliances and stiffnesses (Table 1), the agreement between XRD-stress and DFT is generally good, with maximum discrepancies at around 50%. Our experimental values also agree well with those obtained experimentally on GST124 films by BLS[24] (in GPa, $C_{11} = 47.9, C_{12} = 16.3, C_{44} = 15.8$), especially for the leading terms S_{11} and C_{11}. On the other hand, previous DFT results for GST124[23] (in GPa, $C_{11} = 115, C_{12} = 12.6, C_{44} = 13.3$) differ from the present DFT calculations on GST225. It is not obvious that the elastic constants of GST225 and GST 124 should be the same. A simple bound counting argument suggests that they should be different, but not by that much. Figure 3 displays two contiguous sections of <100> planes for GST124 (5 Ge, 10 Sb and 20 Te) and GST225 (8 Ge, 8 Sb and 20 Te). Young's modulus for a load in a {100} direction is obtained from the second derivative of the bond energy normalized to the area of an atom[40]. Assuming that the Ge-Te and Sb-Te bonds are the same in GST124 and in GST225, and because there are 15 bonds for GST124 and 16 bonds for GST225, one would expect GST225 to be approximately 16/15 stiffer than GST124, much closer than what is suggested by our DFT results.

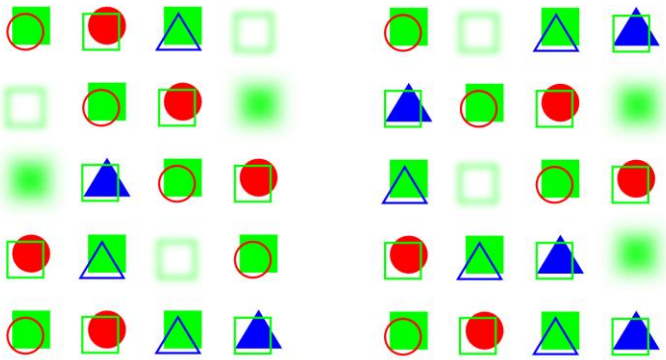

Figure 3. (color online) Interatomic bonds in the <100> directions for a) GST124, b) GST225. Two contiguous 20 atoms sections of <100> planes are represented, the furthest with full symbols, the closest with hollow symbols. Triangles depict Ge atoms, circles Sb atoms and squares Te atoms. Blurred squares, full or hollow, represent unbonded Te atoms and are indicative of a vacancy in the other plane.

The explanation for the much stiffer GST124 results is that in this previous study[23] we reported the full set of elastic constants for a 7 atoms GST124 cell, and, due to symmetry, the positions of the atoms could not be relaxed prior to differentiating the energy to access the stiffnesses. Table 2 displays the elastic constants for relaxed and unrelaxed GST124 and GST225 with 64 and 36 atoms unit cells respectively, and demonstrates why it is important to use large enough unit cells so that ionic relaxation is not prohibited by symmetry in order to obtain accurate elastic coefficients. In both relaxed and unrelaxed cases, GST225 with more bonds is stiffer in the [100] direction than GST124 by factors of 17.85/15 (relaxed) and 15.28/15 (unrelaxed) ($E_{[100]} = 1/S_{11}$), which indicates that the bound counting hypothesis is at best a rough approximation.

Table 2. Elastic properties (compliances, stiffnesses and bulk modulus) of GST225 and GST124 from PAW-DFT with and without ionic relaxation (compliances in TPa^{-1}, Stiffnesses and bulk modulus in GPa).

	GST225		GST124	
	Relaxed	unrelaxed	Relaxed	unrelaxed
S_{11} (TPa^{-1})	18 ± 2	8 ± 1	22 ± 1	8 ± 1
S_{12} (TPa^{-1})	-2 ± 1	-0.3 ± 0.1	-3.5 ±0.8	-0.3 ± 0.1
S_{44} (TPa^{-1})	83 ± 8	61 ± 2	93 ± 6	65 ± 2
C_{11} (GPa)	58 ± 4	125 ± 3	49 ± 2	123 ± 3

C_{12} (GPa)	8 ± 3	4 ± 1	9 ± 1	4 ± 1
C_{44} (GPa)	12 ± 1	16 ± 1	11 ± 1	15 ± 1
K (GPa)	25 ± 1	45 ± 1	23 ± 1	44 ± 1

The only elastic property for which multiple results are available is the bulk modulus K. Published values range from 27 GPa to 58 GPa, a discrepancy of 114%. This discrepancy cannot be attributed solely to methodological differences, as experimentally determined K are 27 GPa (BLS)[24] and 39-41 GPa (XRD)[7, 19], while simulation results vary between 27 GPa and 58 GPa. From the elastic constants determined by XRD-stress, we obtain a value of K at around 20 GPa, with an estimated error of 5 GPa. This result suggests a bulk modulus at the lower end of the scale. This value is also in good agreement with our DFT-PAW results, which predict a value of 25 GPa (±1 GPa). Table 2 also illustrates the effect of atomic relaxation on the bulk modulus: it is significant, as relaxed systems are 80% more compressible than unrelaxed ones. Careful re-examination of previous simulation results confirms that this effect accounts for the larger values of K. With this in mind, we believe that the actual value for K lies between 20 and 30 GPa, as the only remaining outliers are the XRD results from [7] and [19].

For a cubic material, the elastic anisotropy is often described by the Zener ratio $A = 2C_{44}/(C_{11} - C_{12})$; this corresponds to the ratio of the shear moduli in the [100] and [110] directions, and elastic isotropy corresponds to $A = 1$. Our experimental and simulation values for A are in excellent agreement, with values at 0.46 and 0.48 respectively, both slightly lower than 0.5. This suggests that the shear modulus in the [100] direction is lower than the shear modulus in the [110] direction, which is relatively uncommon, especially for crystals with a FCC lattice[27]. For these materials, it is more meaningful to use the Ledbetter anisotropy index A^* to estimate the level of elastic anisotropy. For cubic crystals with $A < 1$, $A^* = 1/A$, which for GST225

gives experimental and theoretical values of 2.17 and 2.11 respectively. From published databases of elastic constants[41], the median Ledbetter index for cubic crystals is 2.08. This suggests that the elastic anisotropy of cubic GST225 is indicative of that of cubic crystals in general, and that GST225 cannot realistically be modelled as an isotropic material. Due to its simplicity, the Zener ratio A is the most often used generic descriptor of elastic anisotropy for cubic crystal systems, but it is certainly not the only possible one. In addition, provided that elastic tensors are available, it is possible to determine the anisotropy of a specific property. The anisotropy of E, defined as the ratio of its maximum by its minimum, is 1.90 for XRD-stress and 1.83 for PAW-DFT. Figures 4(a) and 4(c) display the angular dependence of Young's modulus E in a spherical plot and for a cross section in the $(\bar{1}10)$ plane respectively. For an isotropic material, E would be represented by a sphere. The maximum values occur on-axis at 38 GPa, the minimum values are along the <111> directions at 20 GPa.

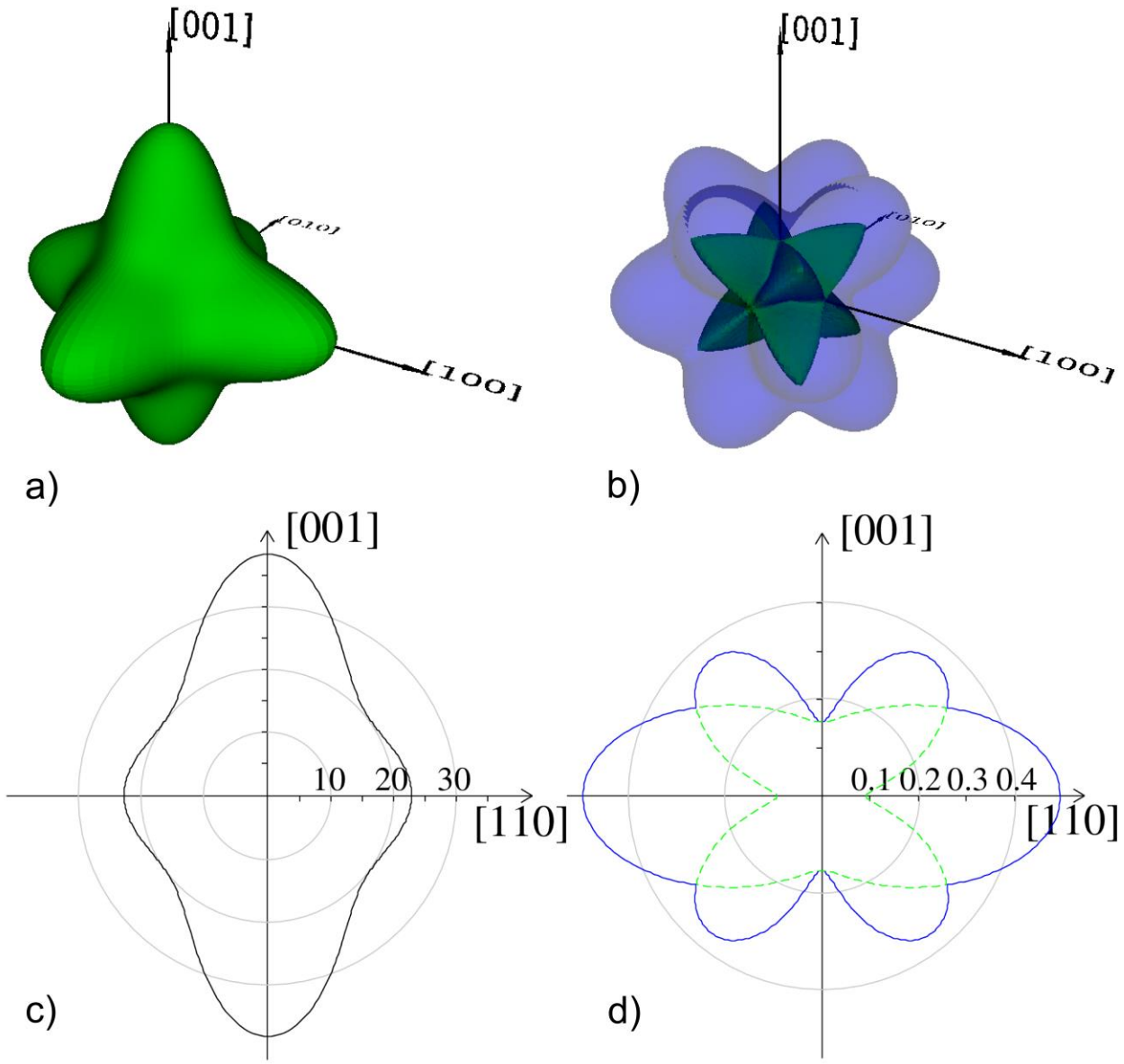

Figure 4. a) Three-dimensional representation of Young's modulus from XRD measurements. The iso-surface gives the value of the Young's modulus for a given direction; b) Three-dimensional representation of Poisson's ratio from XRD, the transparent iso-surface represents the maximum transverse value for a given direction, while the solid iso-surface represents the minimum transverse value; c) sections of a) in the $(\bar{1}10)$ plane; d) section of b) in the same plane, the solid line represents the maximum transverse value for a given direction, while the dashed line represents the minimum transverse value.

Considering the good agreement between stiffness coefficients, it is not surprising that the Young's modulus values also agree well. The XRD-stress value varies between 20 GPa and 39 GPa while the PAW-DFT value varies between 31 GPa and 57 GPa. The only comparable value is 39 GPa, derived from BLS experiments. Such is the importance of the modulus of elasticity, it is very surprising that it has not been measured more often. The biaxial modulus *Y* has been measured and analysed by micromechanical methods such as curvature measurement[8, 11, 22] and nanoindentation[22, 42], and measured values vary between 37 and 59 GPa. In an anisotropic material, *Y* depends on the plane in which the stress is applied, and we obtain values that vary between 25 and 45 GPa with XRD-stress and between 38 and 64 GPa with PAW-DFT.

We are not aware of any measurement or calculations of the shear modulus and of the Poisson's ratio. The measured and calculated values are in good agreement, especially concerning Poisson's ratio for GST225. Both shear modulus and Poisson's ratio are anisotropic, but do not otherwise display any exotic behavior. Figure 4(b) displays in a spherical plot the maximum and minimum values of Poisson's ratio and 4(d) is a cross section of the same in the $(\bar{1}10)$ plane. Both figures illustrate the anisotropy of the Poisson's ratio; the maximum and minimum values are both located along the <110> directions, at 0.49 and 0.09 respectively.

The agreement between the results of simulation and measurements is especially good for the relative value of elastic properties. While the experimental uncertainties associated with the residual stress have a direct impact on the absolute values of elastic constants ($\sigma_{\parallel}$ being a common multiplying factor for S_{11}, S_{12} and S_0 in Eq. 4), the effect of its error is partly cancelled out in the calculation of the relative elastic properties.

4. CONCLUSION

In summary, we have evaluated the elastic properties of FCC phase of GST225 by experimental (XRD and residual stress) and theoretical methods (PAW-DFT). Both set of results are in good agreement and suggest that GST225 is rather compliant, with a bulk modulus around 20 GPa, at the lower end of what had previously been measured or calculated. Both methods also predict significant elastic anisotropy with Zener ratio around 0.5.

In addition to advancing the knowledge of the GST225 crystalline structure, the availability of the elastic tensor will help design constitutive models of phase change materials and improve devices where mechanical properties and stress can influence performance and reliability.

AUTHOR INFORMATION

Corresponding Author

*E-mail address: a.s.h.marmier@exeter.ac.uk

Present Addresses

ACKNOWLEDGMENT

We gratefully acknowledge funding from European FP6 framework program-EXCELL Project NoE 5157032, CSIC (NANO-CONTROL 201060E102), Spanish Ministry MICINN (Consolider FUNCOAT CSD2008-00023) and Junta de Andalucia (TEP217). The authors are grateful to Dr. M. Tonelli of the CIGS of the UniMoRe, Modena, Italy for performing the XRD measurements.

REFERENCES

1. Feinleib, J.; de Neufville, J.; Moss, S. C.; Ovshinsky, S. R. Rapid Reversible Light-Induced Crystallization of Amorphous Semiconductors. *Appl. Phys. Lett.* **1971**, *18*, 254-257.
2. Raoux, S.; Welnic, W.; Ielmini, D. Phase Change Materials and Their Application to Nonvolatile Memories. *Chem. Rev.* **2010**, *110*, 240-267.
3. Pirovano, A.; Pellizzer, F.; Tortorelli, I.; Riganó, A.; Harrigan, R.; Magistretti, M.; Petruzza, P.; Varesi, E.; Redaelli, A.; Erbetta, D. Phase-Change Memory Technology with Self-Aligned Mtrench Cell Architecture for 90nm Node and Beyond. *Solid·State Electron.* **2008**, *52*, 1467-1472.
4. Wuttig, M.; Yamada, N. Phase-Change Materials for Rewriteable Data Storage. *Nature Materials* **2007**, *6*, 824-832.
5. Wong, H. S. P.; Raoux, S.; Kim, S.; Liang, J.; Reifenberg, J. P.; Rajendran, B.; Asheghi, M.; Goodson, K. E. Phase Change Memory. *Proc. IEEE* **2010**, *98*, 2201-2227.
6. Kolobov, A. V.; Haines, J.; Pradel, A.; Ribes, M.; Fons, P.; Tominaga, J.; Steimer, C.; Aquilanti, G.; Pascarelli, S. Pressure-Induced Amorphization of Quasibinary Gete-Sb_2Te_3: The Role of Vacancies. *Appl. Phys. Lett.* **2007**, *91*, 021911.
7. Krbal, M.; Kolobov, A. V.; Haines, J.; Pradel, A.; Ribes, M.; Fons, P.; Tominaga, J.; Levelut, C.; Le Parc, R.; Hanfland, M. Temperature Independence of Pressure-Induced Amorphization of the Phase-Change Memory Alloy $Ge_2Sb_2Te_5$. *Appl. Phys. Lett.* **2008**, *93*, 031918.
8. Kalb, J.; Spaepen, F.; Pedersen, T. P. L.; Wuttig, M. Viscosity and Elastic Constants of Thin Films of Amorphous Te Alloys Used for Optical Data Storage. *J. Appl. Phys.* **2003**, *94*, 4908-4912.

9. Xu, M.; Cheng, Y.; Wang, L.; Sheng, H.; Meng, Y.; Yang, W.; Han, X.; Ma, E. Pressure Tunes Electrical Resistivity by Four Orders of Magnitude in Amorphous $Ge_2Sb_2Te_5$ Phase-Change Memory Alloy. *Proceedings of the National Academy of Sciences* **2012**, *109*, E1055-E1062.
10. Xu, B.; Su, Y.; Liu, Z. G.; Zhang, C. H.; Xia, Y. D.; Yin, J.; Xu, Z.; Ren, W. C.; Xiang, Y. H. Effects of Hydrostatic Pressure on the Electrical Properties of Hexagonal $Ge_2sb_2te_5$: Experimental and Theoretical Approaches. *Appl. Phys. Lett.* **2011**, *98*, 142112.
11. Pedersen, T. P. L.; Kalb, J.; Njoroge, W. K.; Wamwangi, D.; Wuttig, M.; Spaepen, F. Mechanical Stresses Upon Crystallization in Phase Change Materials. *Appl. Phys. Lett.* **2001**, *79*, 3597-3599.
12. Nam, S.-W.; Chung, H.-S.; Lo, Y. C.; Qi, L.; Li, J.; Lu, Y.; Johnson, A. C.; Jung, Y.; Nukala, P.; Agarwal, R. Electrical Wind Force–Driven and Dislocation-Templated Amorphization in Phase-Change Nanowires. *Science* **2012**, *336*, 1561-1566.
13. Kolobov, A.; Krbal, M.; Fons, P.; Tominaga, J.; Uruga, T. Distortion-Triggered Loss of Long-Range Order in Solids with Bonding Energy Hierarchy. *Nature chemistry* **2011**, *3*, 311-316.
14. Lee, J.; Park, H.; Cho, S.; Park, Y.; Bae, B.; Park, J.; Park, J.; An, H.; Bae, J.; Ahn, D. In *Highly Scalable Phase Change Memory with Cvd GeSbTe for Sub 50nm Generation*, VLSI Technology, 2007 IEEE Symposium on, IEEE: 2007; pp 102-103.
15. Im, D.; Lee, J.; Cho, S.; An, H.; Kim, D.; Kim, I.; Park, H.; Ahn, D.; Horii, H.; Park, S. In *A Unified 7.5 Nm Dash-Type Confined Cell for High Performance PRAM Device*, Electron Devices Meeting, 2008. IEDM 2008. IEEE International, IEEE: 2008; pp 1-4.
16. Yu, B.; Sun, X.; Ju, S.; Janes, D. B.; Meyyappan, M. Chalcogenide-Nanowire-Based Phase Change Memory. *Nanotechnology, IEEE Transactions on* **2008**, *7*, 496-502.
17. Longo, M.; Fallica, R.; Wiemer, C.; Salicio, O.; Fanciulli, M.; Rotunno, E.; Lazzarini, L. Metal Organic Chemical Vapor Deposition of Phase Change Ge1Sb2Te4 Nanowires. *Nano Lett.* **2012**, *12*, 1509-1515.
18. Giusca, C. E.; Stolojan, V.; Sloan, J.; Börrnert, F.; Shiozawa, H.; Sader, K.; Rümmeli, M. H.; Büchner, B.; Silva, S. R. P. Confined Crystals of the Smallest Phase-Change Material. *Nano Lett.* **2013**, *13*, 4020-4027.
19. Kolobov, A. V.; Haines, J.; Pradel, A.; Ribes, M.; Fons, P.; Tominaga, J.; Katayama, Y.; Hammouda, T.; Uruga, T. Pressure-Induced Site-Selective Disordering of $Ge_2Sb_2Te_5$: A New Insight into Phase-Change Optical Recording. *Phys. Rev. Lett.* **2006**, *97*, 035701.
20. Caravati, S.; Bernasconi, M.; Kuhne, T. D.; Krack, M.; Parrinello, M. Unravelling the Mechanism of Pressure Induced Amorphization of Phase Change Materials. *Phys. Rev. Lett.* **2009**, *102*, 205502.
21. Zhou, J.; Sun, Z. M.; Xu, L. H.; Ahuja, R. Effect of Dopants on the Structure and Properties of $Ge_2Sb_2Te_5$ Studied by Ab Initio Calculations. *Solid State Commun.* **2008**, *148*, 113-116.
22. Park, I. M.; Jung, J. K.; Ryu, S. O.; Choi, K. J.; Yu, B. G.; Park, Y. B.; Han, S. M.; Joo, Y. C. Thermomechanical Properties and Mechanical Stresses of $Ge_2Sb_2Te_5$ Films in Phase-Change Random Access Memory. *Thin Solid Films* **2008**, *517*, 848-852.
23. Marmier, A.; Kohary, K.; Wright, C. D. Determination of the Anisotropic Elastic Properties of $Ge_1Sb_2Te_4$. *Appl. Phys. Lett.* **2011**, *98*, 231911.

24. Blachowicz, T.; Beghi, M. G.; Guntherodt, G.; Beschoten, B.; Dieker, H.; Wuttig, M. Crystalline Phases in the GeSb2Te4 Alloy System: Phase Transitions and Elastic Properties. *J. Appl. Phys.* **2007**, *102*, 093519.
25. Sa, B.; Zhou, J.; Ahuja, R.; Sun, Z. First-Principles Investigations of Electronic and Mechanical Properties for Stable $Ge_2Sb_2Te_5$ with Van der Waals Corrections. *Computational materials science* **2014**, *82*, 66-69.
26. Reuss, A. Berechnung Der Fließgrenze Von Mischkristallen Auf Grund Der Plastizitätsbedingung Für Einkristalle. *Zeitschrift für Angewandte Mathematik und Mechanik* **1929**, *9*, 49-58.
27. Gressmann, T.; Wohlschlögel, M.; Shang, S.; Welzel, U.; Leineweber, A.; Mittemeijer, E.; Liu, Z.-K. Elastic Anisotropy of Γ′-Fe_4N and Elastic Grain Interaction in Γ′-Fe_4N_{1-Y} Layers on A-Fe: First-Principles Calculations and Diffraction Stress Measurements. *Acta Mater.* **2007**, *55*, 5833-5843.
28. Stoney, G. G. The Tension of Metallic Films Deposited by Electrolysis. *Proceedings of the Royal Society of London. Series A, Containing Papers of a Mathematical and Physical Character* **1909**, *82*, 172-175.
29. Janssen, G. Stress and Strain in Polycrystalline Thin Films. *Thin Solid Films* **2007**, *515*, 6654-6664.
30. Yamada, N.; Matsunaga, T. Structure of Laser-Crystallized $Ge_2Sb_{2+X}Te_5$ Sputtered Thin Films for Use in Optical Memory. *J. Appl. Phys.* **2000**, *88*, 7020-7028.
31. Welzel, U.; Ligot, J.; Lamparter, P.; Vermeulen, A.; Mittemeijer, E. Stress Analysis of Polycrystalline Thin Films and Surface Regions by X-Ray Diffraction. *J. Appl. Crystallogr.* **2005**, *38*, 1-29.
32. Kresse, G.; Furthmuller, J. Efficiency of Ab-Initio Total Energy Calculations for Metals and Semiconductors Using a Plane-Wave Basis Set. *Computational Materials Science* **1996**, *6*, 15-50.
33. Kresse, G.; Furthmuller, J. Efficient Iterative Schemes for Ab Initio Total-Energy Calculations Using a Plane-Wave Basis Set. *Physical Review B* **1996**, *54*, 11169-11186.
34. Kresse, G.; Hafner, J. Abinitio Molecular-Dynamics for Liquid-Metals. *Physical Review B* **1993**, *47*, 558-561.
35. Kresse, G.; Hafner, J. Ab-Initio Molecular-Dynamics Simulation of the Liquid-Metal Amorphous-Semiconductor Transition in Germanium. *Physical Review B* **1994**, *49*, 14251-14269.
36. Marmier, A.; Lethbridge, Z. A. D.; Walton, R. I.; Smith, C. W.; Parker, S. C.; Evans, K. E. ElAM: A Computer Program for the Analysis and Representation of Anisotropic Elastic Properties. *Comput. Phys. Commun.* **2010**, *181*, 2102-2115.
37. Sun, Z.; Zhou, J.; Ahuja, R. Structure of Phase Change Materials for Data Storage. *Phys. Rev. Lett.* **2006**, *96*, 055507.
38. Lee, G.; Jhi, S.-H. Ab Initio Studies of Structural and Electronic Properties of the Crystalline $Ge_2sb_2te_5$. *Physical Review B* **2008**, *77*, 153201.
39. Tsafack, T.; Piccinini, E.; Lee, B.-S.; Pop, E.; Rudan, M. Electronic, Optical and Thermal Properties of the Hexagonal and Rocksalt-Like $Ge_2Sb_2Te_5$ Chalcogenide from First-Principle Calculations. *J. Appl. Phys.* **2011**, *110*, 063716.
40. Ashby, M. F.; Jones, D. R. H., *Engineering Materials 1: An Introduction to Their Properties and Applications*; Butterworth-Heinemann: Oxford, 2011.

41. Every, A. G.; McCurdy, A. K., Low Frequency Propertie of Dielectric Crystals. In *Landolt-Börnstein, Numerical Data and Functional Relationships in Science and Technology*, Springer Verlag: Berlin, 1993; Vol. 29a.
42. Jong, C. A.; Fang, W. L.; Lee, C. M.; Chin, T. S. Mechanical Properties of Phase-Change Recording Media: GeSbTe Films. *Japanese Journal of Applied Physics Part 1-Regular Papers Short Notes & Review Papers* **2001**, *40*, 3320-3325.

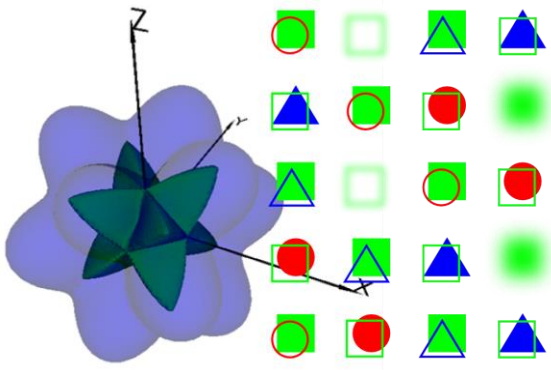

TOC Image